ADDITIVE MANUFACTURING OF MULTI-FUNCTIONAL LATTICE STRUCUTRE-BASED CONCEPTS FOR THERMAL PROTECTION SYSTEM

Yu-Chuen Chang[1], Hao Wu[2], Colin Yee[1], Roderick Reber[3], Jon Langston[1], Steven Kim[1,2], Joseph H. Koo[1,2]
[1]Department of Mechanical Engineering, The University of Texas at Austin
Austin, TX/USA

[2]KAI, LLC.
Austin, TX/USA

[3]Arkema Inc.
King of Prussia, PA/USA

ABSTRACT

The potential of lattice structure as a dual-layer meta-material for ablative thermal protection system (A-TPS) was investigated. The geometry of the dual-layer sample comprises a solid Polyether-ketone-ketone (PEKK) recession layer (RL) and a lattice-structure insulating layer (IL). The lattice structure was printed by Fused Filament Fabrication (FFF) process and designed with three different topologies (3D honeycomb, Gyroid, and Schwarz D) with different relative densities (50% and 70%). The dual-layer lattice structures were tested in Oxy-Acetylene Test Bed (OTB) with 100 W/cm^2 heat flux for 30 seconds. The temperatures at the end of RL and IL were compared and the feasibility of using lattice structure as light weight heat insulation material was validated. The results can integrate with impact absorption properties of lattice structure and optimize the performance of TPS for various mission requirements.

1. INTRODUCTION

The advancement of Additive Manufacturing (AM) allows for producing complex geometry and printing material with multiple properties in a single process. Therefore, it could potentially be applied to optimize the design of the ablative thermal protection system (A-TPS) for various space missions. The A-TPS is often a polymetric ablatives, which is a combination of recession layer (RL) with high thermal capacity and an underlying thermal insulating layer (IL) to protect space vehicle from the aerodynamic heating. Recently, Milos et. al. [1] developed a new dual-layer woven carbon/phenolic for Heatshield for Extreme Entry Environment Technology (HEEET) project and changed the thickness of each layer to reduce the A-TPS mass. In this study, the potential of the AM process (*e.g.*, Fused Filament Fabrication, FFF) for the dual-layer A-TPS application was investigated, since the AM technology might provide greater flexibility to optimize the mechanical-thermal properties of materials.

Mechanical-thermal behavior is the primary consideration for designing A-TPS. The A-TPS needs to be lightweight and barrier of the aerodynamic heating loads for the space application. The

RL serves as direct jet impingement resistant purpose and requires high ablation resistance, high decomposition temperature, and moderate thermal conductivity [2]. The IL maintains the interior temperature of the space vehicle and is typically low density and low thermal conductivity [1-2]. The design of lattice structure by FFF potentially enable to use the same material but vary the material properties for RL and IL. Catchpole-Smith et. al. [4] studied the change of thermal conductivity of three different lattice structures (gyroid, Schwarz D, and Schwarz P) made by Hastelloy-X and Ti6Al4V for the heat exchanger application. They interpreted the effective thermal conductivity of lattice structure as the function of solid material properties and volume fraction. Additionally, under the same volume frication, gyroid and Schwarz D structure provides lower thermal properties than Schwarz P. Habib et. al. [5] investigated bending, buckling, and stretch dominated structure and found the bending-based structures have lower stiffness and compression yield strength but better energy absorption. The stretch and buckling-based structures perform stiffer and stronger but have less capability to absorb energy. Maskery et. al. [6] also found Schwarz P (stretch and buckling-dominated architecture) has higher elastic modulus than Schwarz D and gyroid (bending architecture). In general, the increment of volume fraction will increase mechanical strength but also the thermal conductivity [3]. It is necessary to determine the trade-off between mechanical and thermal conductivity properties for A-TPS application.

To evaluate the feasibility of applying lattice structure on A-TPS designs, this study examined the heat insulation performance of dual-layer lattice structure by the OTB test. The RL of OTB specimen was solid for enhanced ablation resistance, and the IL was investigated with different lattice structures. The heat insulation capacity of lattice structure with various cell topologies and densities was experimentally determined by collecting temperature gradients conforming to ASTM E285-08. Additionally, the energy absorption performance of the lattice structures was characterized to better understand thermo-mechanical properties. The data collected enable us to demonstrate the efficiency of the lattice structure-based concept for A-TPS in the future research.

2. EXPERIMENTATION

2.1 Lattice Designs

Gyroid, Schwarz D, and 3D honeycomb were the three selected lattice structures in this study. Gyroid and Schwarz D are minimal surfaces and have good energy absorption properties [6]. Additionally, they have lower thermal conductivity in the family of minimal surfaces [4]. The lattice structure of 3D honeycomb represented the closed cell type, which is widely used for heat insulation in the industry [7]. The honeycomb structure is also bending-dominated and provides an energy absorption behavior.

The lattice structures were generated using infill function in ANSYS SpaceClaim and exported the files as STL (STereoLithography). The parameters to generate lattice structures are length l, wall thickness t, and relative density ρ. It should be noticed that the definition of length setup in SpaceClaim is “the spacing between the walls” instead of “length of unit cell”. The term of l in this study followed the definition in SpaceClaim. The wall thickness of unit cells could vary the effective thermal conductivity of a lattice structure even at the equivalent level of density [4], hence the wall thickness kept constant for most of compression and OTB tests. All specimens were built using FFF process. Due to the precision of the FFF machine used in this study, the geometric precision was constrained to 0.1 mm.

2.2 Compression Test

2.2.1 Specimen designs and manufacturing

The lattice-structure specimens for compression tests were 5.08- × 5.08- × 2.54-cm (2- × 2- × 1-inches) cuboids conforming to ASTM D1621. All specimens were designed with 1 mm wall thickness and 25% of relative density. The range of relative density is recommended by Gibson et. al. [7]. Due to the precision limitation, the actual relative densities are slightly different between each unit cell type. Table 1 summarizes the geometric parameters of compression test samples.

Table 1. Specimen geometries of compression test

Unit Cell Type		**Cell Design Parameters**			**Overall Specimen**
		l (mm)	t (mm)	ρ^* (SpaceClaim)	
3D Honeycomb	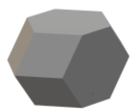	5	1	24.5%	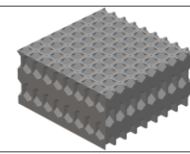
Gyroid		2.5	1	24.7%	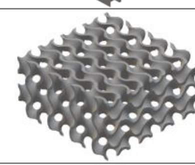
Schwarz D		3.1	1	24.6%	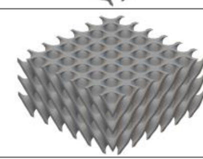

*: The density ρ is the modeling density shown in ANSYS SpaceClaim.

The specimens were produced using Craftbot XL 3D printers from polylactide (PLA) filament (procured form H&H 3D Plastics, https://www.hh3dplastics.com/). The print bed was parallel to the x-y plane. The FFF setting for PLA in this study was 215℃ for the printing nozzle and 60℃ for the print bed. The maximum speed of the printing was 120 mm/s. The printing infill is 100%. Figure 1 shows the printed specimens with three different lattice structures.

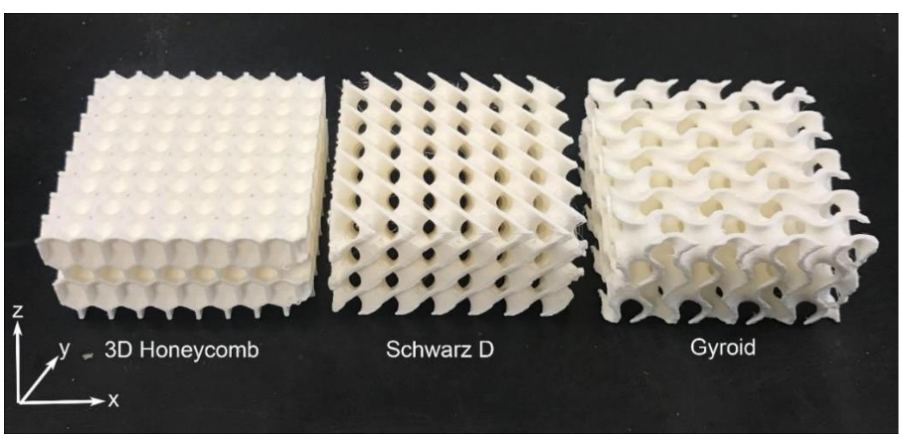

Figure 1. Compression test specimens produced by Craftbox XL 3D printer.

2.2.2 Compression apparatus

The compression tests were conducted with Instron 1125 of capability 20,000 lbf (88.96 kN) and followed the guidance of ASTM D1621. The specimens laid on the compression plate in x-y plane and were compressed in z direction. The testing speed was set to 0.2 in/min (5.08 mm/min). A compression test was continued until the densification regions were reached. Three replicates of lattice structures were tested in this study. The initial collected data were displacement versus force and postprocessed to stress and strain curve with theoretical dimensions of samples in Microsoft Excel. Figure 2 shows the example of setup and orientation of the compression test.

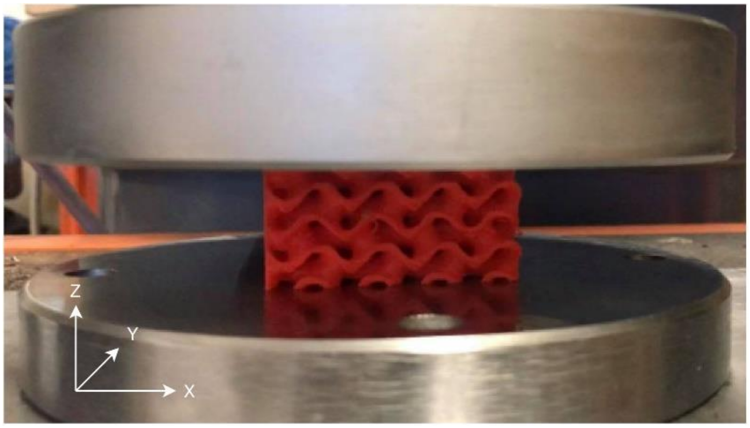

Figure 2. Compression test setup and specimen orientation.

2.3 OTB Test

2.3.1 Dual-layer lattice specimens

The specimens of OTB tests were 30-mm diameter × 30-mm thick dome-shapes. The OTB specimens had a 21-mm extruded hole with 2.54-mm of diameter to insert the thermocouples. The thickness ratio of the RL and IL was 3:7, which is close to the thickness ratio in NASA's Heatshield for Extreme Entry Environment Technology (HEEET) project [1]. The ablative RL was 100% infill, and the IL was designed as lattice structures with 1 mm of outside wall thickness. Figures 3 and 4 illustrate the drawing and photography of the OTB specimens.

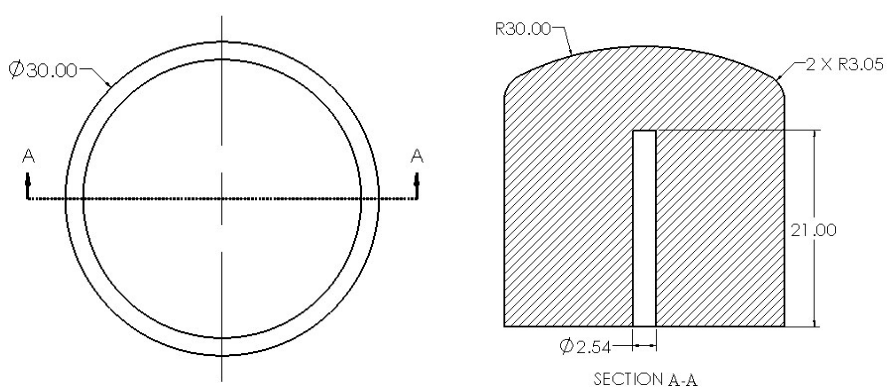

Figure 3. Overall dimensions of OTB specimens (*Left*) Top view (*Right*) Side view.

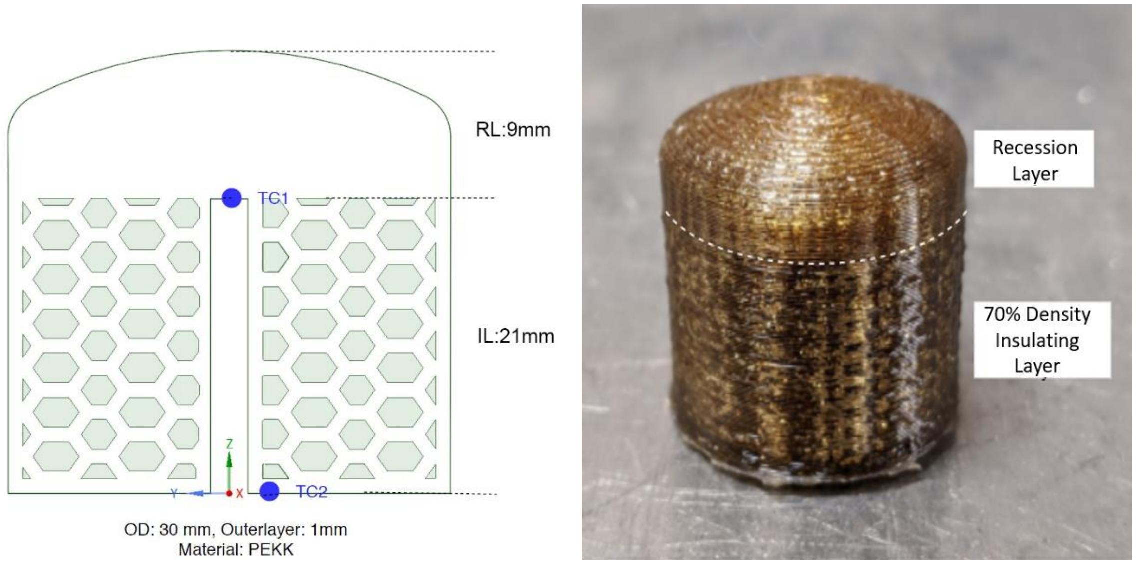

Figure 4. (*Left*) Illustration of OTB specimen designs and (*Right*) Sample D1 of dual-layer OTB test (the white dashed line was added to highlight boundary of RL and IL).

Cell topology and relative density have critical impact on the heat insulation capacity [4,7] and were examined in this study. Table 2 summarizes the designs of specimens for OTB tests. Sample R1 represented the reference material, which is solid for both RL and IL. The purpose of Sample D was to test material with the same cell topology and wall thickness but different densities. Cell D1 and D2 were 3D honeycomb with 70% and 50% of density. Sample T aimed to investigate the impact of different cell topologies with the same density and wall thickness. Cell T1 and T2 were gyroid and Schwarz D with 50% of density. Sample C was to study the influence from the wall thickness/cell size. In our study, C1 and D2 had the same cell topology (3D honeycomb) and density (48.8%) but different wall thickness/cell size.

Table 2. Design parameters of the lattice-structure insulating layers

Name	Cell structure	Spacing between the walls l (mm)	Min. wall thickness t (mm)	Ideal relative density	Modeling relative density ρ*
R1	Solid	-	-	100%	100%
D1	3D honeycomb	1	1	70%	70.4%
D2	3D honeycomb	2	1	50%	48.8%
T1	Gyroid	1.27	1	50%	48.6%
T2	Schwarz D	1.57	1	50%	48.6%
C1	3D honeycomb	4	2	50%	48.8%

*Due to constraints of minimum printable features, the density ρ would vary slightly than ideal density.

2.3.2 Material and manufacturing

Polyether-ketone-ketone (PEKK) is the high-temperature thermoplastic with high strength-to-weight ratio and low flammability [8]. As a member of the polyaryletherketone (PAEK) family, PEKK has high temperature stability [9]. For example, Tadini et. al. [9] studied the chemical degradation behavior of carbon/PEKK and carbon/phenolic composites in 30°C to 1000°C and found that carbon/PEKK degraded at the higher temperature. Wu et. al. [8] compared the ablation performance of PEKK, PEEK (Polyether-ether-ketone), and PEI (Polyetherimide). The results of Thermogravimetric Analysis (TGA) and Micro-scale Combustion Calorimetry (MCC) tests indicate that PEKK has highest char yield, lower heat release capacity, and so better flame-resistance property. The specimens of OTB tests were produced by Arkema Inc. with Ultimaker 3S printer and Kepstan ® 7002 PEKK filament. Table 3 presents the material properties of PEKK properties at room temperature.

Table 3. Thermal properties of PEKK at 23 ℃

Property	PEKK	Ref.
Density, g/cm^3	1.29	[10]
Thermal conductivity, W/(m·k)	0.23	[11]*
Heat capacity, J/(g·K)	1.02	[10]
Melting temperature, ℃	331~334	[10]
Glass transient temperature, ℃	162	[10]

*Thermal conductivity of PEKK is obtained by the regression result in [11].

2.3.3 OTB apparatus

The oxyacetylene test bed (OTB) utilizes a welding torch nozzle which mixes compressed oxygen and acetylene to generate a high heat flux, high speed flowfield for aerothermal testing of ablative materials. The OTB used for these tests is pictured below in Figure 5. A combination of radiative and convective heat flux is generated by the torch and applied to a test model held in place with a vice in order to simulate an extreme oxidative environment, such as solid rocket exhaust plumes [12]. The heat flux applied to the test model is varied by adjusting the oxygen to acetylene flow rate ratio and the test model’s standoff distance from the nozzle and is calibrated using a Gardon gage.

Figure 5. Unshielded glass/phenolic test model undergoing OTB testing.

OTB testing is advantageous and cost effective tool as it provides a large amount of data from a single test, including surface temperature, back-side/heat soaked temperature, in-depth temperature, mass change, volume change, depth of ablation, ablation rate, and pyrolysis zone depth. Morphological and compositional changes in the charred and pyrolyzing material can be examined after testing.

For this series of experiments, a carbon/carbon heatshield was glued to the PEKK test models using Aremco's GraphiBond high-temperature carbon adhesive. A 31-mm diameter hole in the center of the heat shield permits heating to be applied to the solid dome portion of the test model while minimizing sidewall heating by deflecting flow out and away from the rest of the test model. The modified OTB test setup is shown in Figure 6. The insulative nature of the GraphiBond minimized heat transfer between the heat shield and the test model in order to prevent additional heating affects from the larger surface area or cooling affects due to heat sinking during the heat-soaked portion of the tests.

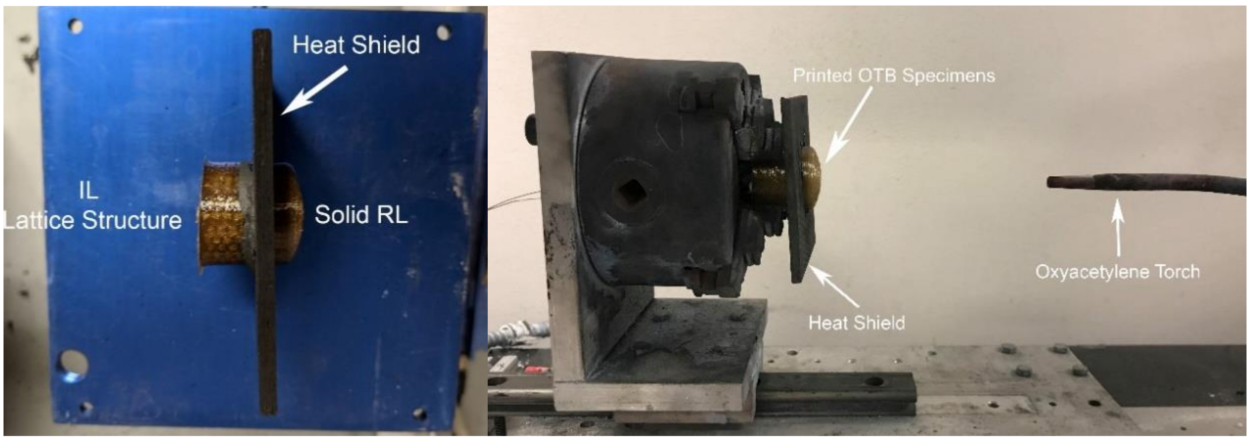

Figure 6. Modified OTB test sample and experimental setup.

One K-type thermocouple (TC1) was positioned at the back side of the solid dome while a second TC (TC2) was positioned at the back side of the metamaterial portion in order to determine the temperature difference across the metamaterial backing section and determine the peak heat-soaked time for each section of the PEKK test model (see Figure 3). The OTB applied a 100 W/cm^2 heat flux for 30 seconds to the solid dome of the 30 mm diameter, 30 mm thick PEKK test models. After 30 seconds, the test model was removed from the flowfield and TC temperature measurements continued until the peak heat-soaked time was detected.

3. RESULTS AND DISCUSSION

3.1 Compression Test

The stress-strain curve (σ-ε curve) of lattice structures shown in Figure 7 has three regions: an elastic region (stage I), a plateau region (stage II), and densification region (stage III). When the compressive load is applied, the cell wall of lattice structures bends at lower stress initially and provides a linear elastic deformation. When the compressive force is higher than a certain level, the cell wall begins collapsing due to elastic buckling (*e.g.,* elastomer), plastic yielding (*e.g.,* metal), or brittle crushing (*e.g.,* ceramic). The collapsing process of lattice structure causes a significant increase in compressive strain, but the stress maintains nearly constant, which is so-called plateau region. The plateau region allows greater absorption of impact energy without noticeable increment of the load on lattice structures. The cell walls will keep collapsing until they contact each other. In subsequent densification region, the lattice structure performs like a parent material and the stress increases rapidly [5,7].

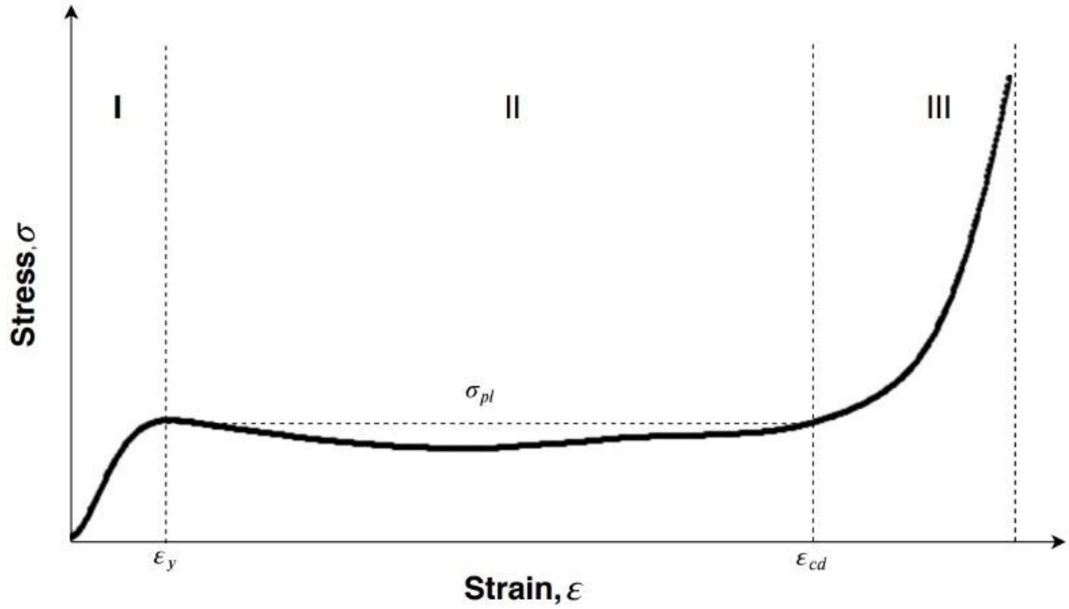

Figure 7. Schematic of compressive stress-strain curve for cellular materials (I), elastic region (II), and plateau region (III) densification region (modified from [5]).

The energy absorption diagram [7] is commonly used to determine the boundary of the plateau and densification region. It describes the relation between the peak stress and absorbed energy W in the specific range of strain ε. The absorbed energy W is equivalent to the area of σ-ε curve [13] and defined as

$$\boldsymbol{W = \int_0^{\varepsilon} \sigma(\varepsilon) d\varepsilon} \quad (1)$$

The plateau stress σ_{pl} is another important parameter to observe the energy absorption property of lattice structure. The plateau stress defined the average of stress in the plateau region [14] (between yield strain ε_y and critical strain at the end of plateau region ε_{cd}) as shown in Figure 7. The plateau stress is given by

$$\boldsymbol{\sigma_{pl} = \frac{\int_{\varepsilon_y}^{\varepsilon_{cd}} \sigma(\varepsilon) d\varepsilon}{\varepsilon_{cd} - \varepsilon_y}} \quad (2)$$

where the yield strain ε_y is obtained by the peak stress of the elastic region. The energy absorption efficiency η represents the ratio of actual energy absorption to the critical stress σ_{cd} at the end of plateau region [5,13] and described as

$$\boldsymbol{\eta(\varepsilon) = \frac{1}{\sigma_{cd}} \int_0^{\varepsilon_{cd}} \sigma(\varepsilon) d\varepsilon} \quad (3)$$

Figure 8 shows the compression test results for the selected lattice structures and examples of energy-absorption diagram (*right* column in Figure 8).

A. 3D Honeycomb at 25% of the density

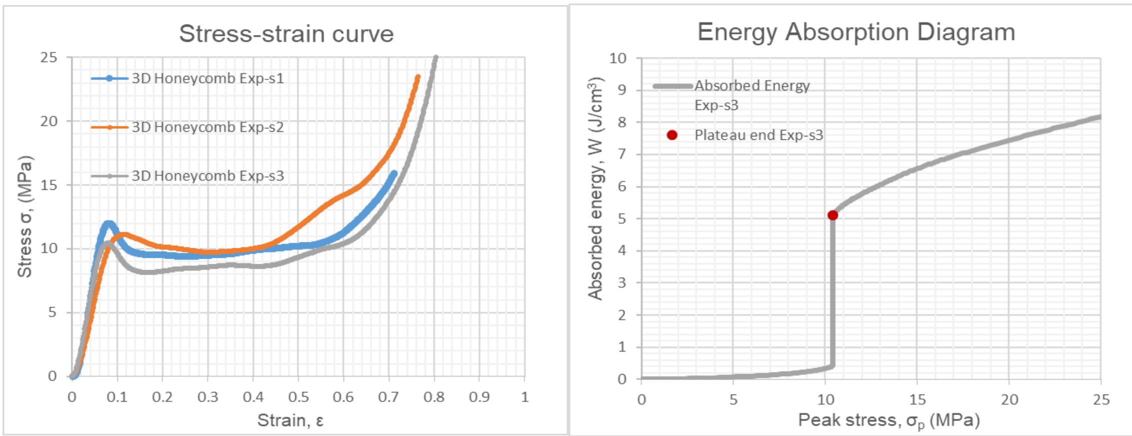

B. Schwarz D at 25% of the density

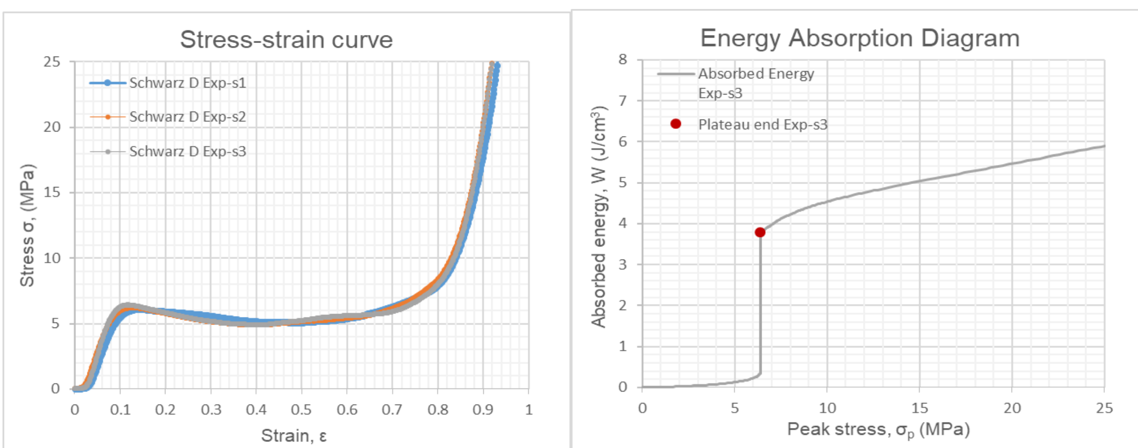

C. Gyroid at 25% of the density

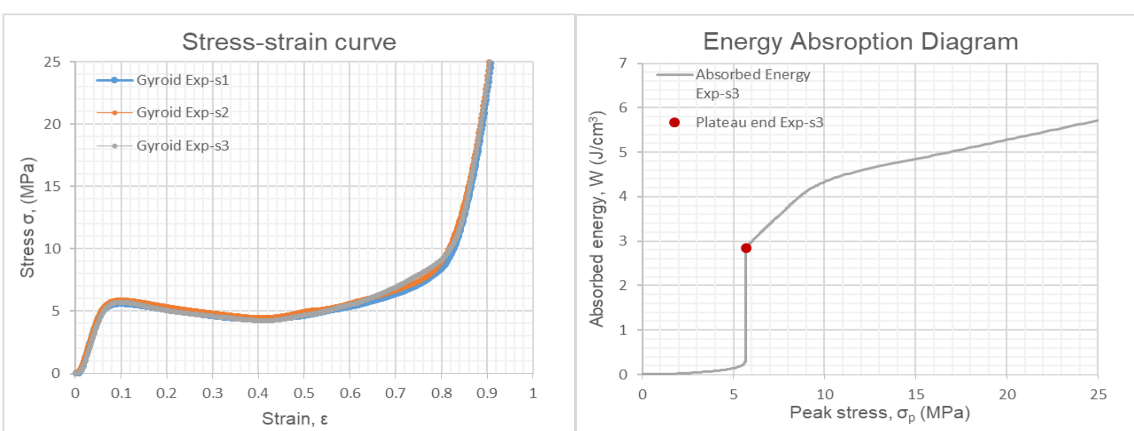

Figure 8. Compression stress-strain curves and representative energy absorption diagrams for the 3D printed PLA lattice structures with different cell topologies (a. 3D Honeycomb, b. Schwarz, and c. Gyroid).

Table 4 summarizes the average compressive properties of three different lattice structures. The stress-strain curves of gyroid and Schwarz D are similar and have a longer plateau region than 3D honeycomb. The strain at the end of the plateau region is 0.71 for Schwarz D and 0.64 for gyroid. However, both of them also has lower plateau stress than 3D honeycomb. The average plateau stress for Schwarz D and gyroid is 5.43 MPa and 4.95 MPa, respectively. Additionally, the range of plateau region in our test generally agrees with the experimental data in [6]. Overall, the 3D honeycomb structure has the best compressive properties. The 3D honeycomb has the highest plateau stress (9.69 MPa) and absorbed the largest amount of energy (5.15 J/cm^3).

Table 4. Average energy absorption properties of 3D-printed lattice structures

Lattice structure	Plateau stress σ_{pl} (MPa)	Critical strain ε_{cd}	Critical stress σ_{cd} (MPa)	Absorbed Energy W (J/cm^3)	η (%)
3D Honeycomb	9.69	0.57	11.18	5.15	47.82
Schwarz D	5.43	0.71	6.21	3.57	58.02
Gyroid	4.95	0.64	5.72	2.94	51.81

3.2 OTB Test

Figure 9 shows the temperature profiles of TC1 and TC2. During OTB test, the temperature of TC1 for most of the sample rapidly increased in the first 30 sec due to the high heat flux. The solid reference, R1, experienced a thermal shock as high as 80℃. The thermal shock for sample D1 (3D honeycomb with 70% of density) was around 55℃. Sample D2 (3D honeycomb with 50% of density) did not show significant thermal shock within the operating time. Similar behavior were obtained from sample T1 (gyroid with 50% of density). Sample T1 also showed a smooth temperature curve from the TC1. This characteristic explains that a lattice structure with high porosity can provide a better thermal shock resistance. Furthermore, wall thickness/cell size has impact on the thermal shock resistance. Sample D1 and C1 have the same density and cell topology, but the wall thickness of sample C1 is doubled and so does cell size. Although the density of sample C1 is only 50% of D1, it still experienced a thermal shock of 67℃. The temperature profiles of TC1 suggest that the ideal designs for thermal shock resistance prefer lower density and smaller wall thickness/cell sizes.

Table 5 summarizes OTB data for the five different IL designs. The initial mass in Table 5 refers to the gross mass of the OTB specimen, heat shield, and high temperature carbon adhesive, and they were compared with the residual mass after heating. An IR camera was used to record the average surface temperature. The residual mass of all five specimens are similar. The temperature from TC2 demonstrates the good insulation capability of the lattice structures: lower temperature is preferred. Most of the lattice structures had higher TC2 temperature except sample C1. It could be due to the lattice structure has lower mass capacitance compared to solids. Therefore, although the D1, D2, and T1 lattice structure has lower thermal conductivity [4], it might have higher thermal diffusivity due to the decrease of density. Before getting into a concrete conclusion, a primary improvement of the experimental setup is required: during the experiments, the dome of sample R1 and C1 melted and separated from the rest of the specimens. To prevent this melt and drip behavior, all printed OTB specimens will be post cured to improve their crystallinity. Additionally, the data recording in sample T2 was incomplete, and additional tests are needed.

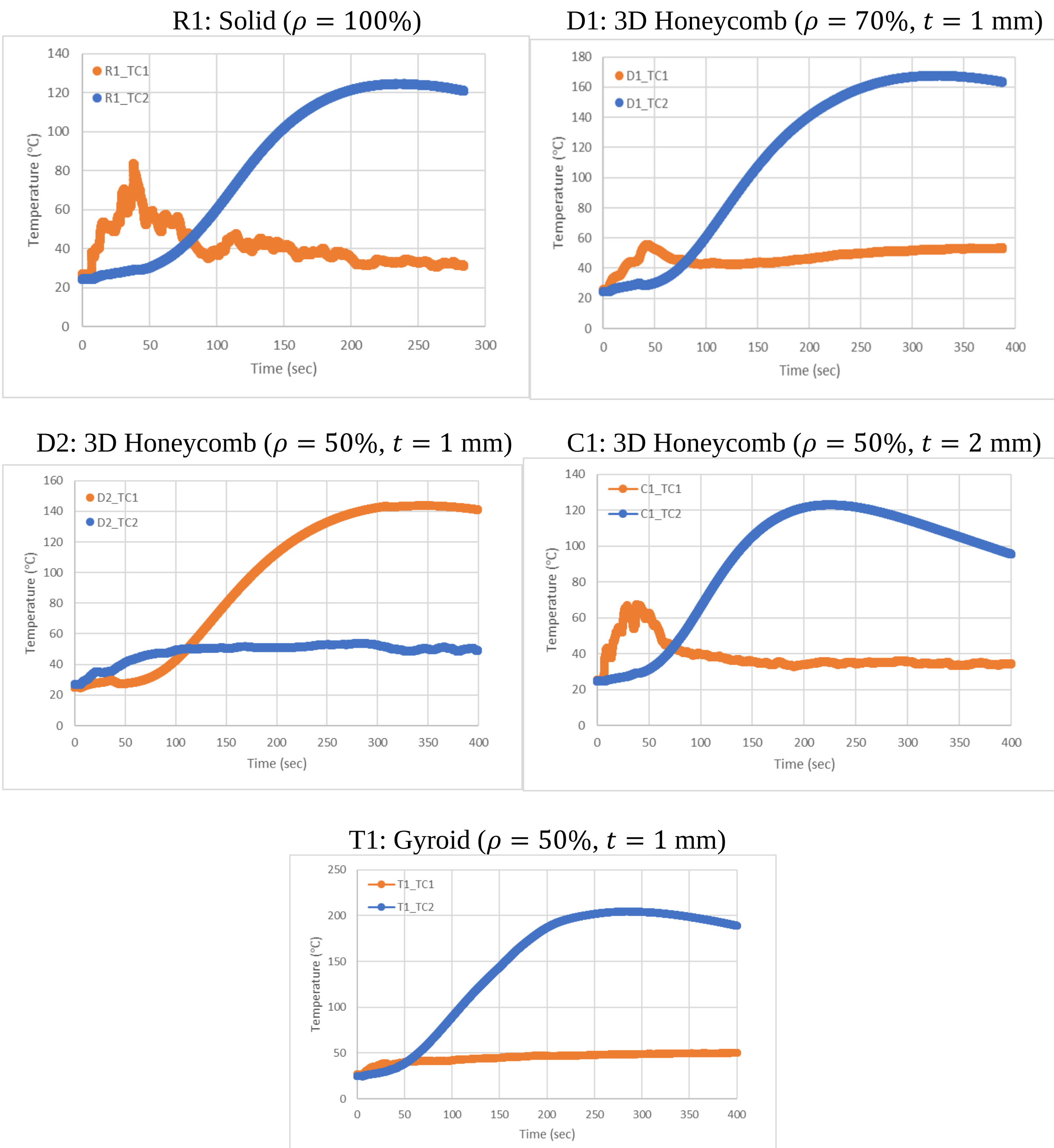

Figure 9. The measured temperature for the back of solid dome (TC1) and heat-soaked temperature (TC2) with different IL designs.

Table 5. Summary of the OTB data with five lattice structure designs

v	Initial mass (g)	Final mass (g)	Residual mass (%)	Average surface temperature (℃)	Max. TC1 (℃)	Max. TC2 (℃)
R1	54.4	53.2	97.8	1588	83.6	124.6
D1	49.3	48.1	97.6		55.7	167.8
D2	50.8	49.5	97.5		54.1	143.9
C1	51.8	50.7	98.0		67.5	123.1
T1	48.8	47.4	97.2		50.6	204.6

4. CONCLUSIONS

This study evaluated the feasibility of using lattice structures for the insulating layer (IL) design of thermal protection systems. For mechanical properties, the 3D honeycomb can absorb more energy than gyroid and Schwarz D and has higher plateau stress. The results of OTB tests show that a lower density and smaller cell size lattice structure provides a better thermal shock resistance. However, the OTB data indicate that the lattice structure also has lower mass capacitance and increase the overall thermal diffusivity. Therefore, future research will explore the possibility to maintain the low thermal conductivity but increase the density of lattice structure to achieve the low diffusivity for this application.

5. REFERENCES

1. Milos, F. S., Chen, Y. K., & Mahzari, M. (2018). Arcjet Tests and Thermal Response Analysis for Dual-Layer Woven Carbon Phenolic. Journal of Spacecraft and Rockets, 55(3), 712-722. doi: https://doi.org/10.2514/1.A34142
2. Kumar, S., & Mahulikar, S. P. (2016). Selection of materials and design of multilayer lightweight passive thermal protection system. Journal of Thermal Science and Engineering Applications, 8(2). doi: https://doi.org/10.1115/1.4031737
3. Natali, M., Kenny, J. M., & Torre, L. (2016). Science and technology of polymeric ablative materials for thermal protection systems and propulsion devices: A review. Progress in Materials Science, 84, 192-275. doi: https://doi.org/10.1016/j.pmatsci.2016.08.003
4. Catchpole-Smith, S., Sélo, R. R. J., Davis, A. W., Ashcroft, I. A., Tuck, C. J., & Clare, A. (2019). Thermal conductivity of TPMS lattice structures manufactured via laser powder bed fusion. Additive Manufacturing, 30. doi: https://doi.org/10.1016/j.addma.2019.100846
5. Habib, F. N., Iovenitti, P., Masood, S. H., & Nikzad, M. (2018). Fabrication of polymeric lattice structures for optimum energy absorption using Multi Jet Fusion technology. Materials & Design, 155, 86-98. doi: https://doi.org/10.1016/j.matdes.2018.05.059
6. Maskery, I., Sturm, L., Aremu, A. O., Panesar, A., Williams, C. B., Tuck, C. J., ... & Hague, R. J. (2018). Insights into the mechanical properties of several triply periodic minimal surface lattice structures made by polymer additive manufacturing. Polymer, 152, 62-71. doi: https://doi.org/10.1016/j.polymer.2017.11.049

7. Gibson, L. J., & Ashby, M. F. (1999). Cellular solids: structure and properties. Cambridge University Press, Cambridge, UK. doi: https://doi.org/10.1017/CBO9781139878326
8. Wu, H., Kafi, A., Yee, C., Atak, O., Langston, J. H., Reber, R., ... & Koo, J. H. (2020). Ablation Performances of Additively Manufactured High-Temperature Thermoplastic Polymers. AIAA-2020-1125, AIAA SciTech 2020 Forum, Orlando, FL. doi: https://doi.org/10.2514/6.2020-1125
9. Tadini, P., Grange, N., Chetehouna, K., Gascoin, N., Senave, S., & Reynaud, I. (2017). Thermal degradation analysis of innovative PEKK-based carbon composites for high-temperature aeronautical components. Aerospace Science and Technology, 65, 106-116. doi: https://doi.org/10.1016/j.ast.2017.02.011
10. Arkema Inc. (2012). Kepstan by Arkema: Technical Data – 7000 Series. Retrieved January 26, 2020 from https://www.arkema.com/export/shared/.content/media/downloads/products-documentations/incubator/arkema-kepstan-7000-tds.pdf
11. Coulson, M., Dantras, E., Olivier, P., Gleizes, N., & Lacabanne, C. (2019). Thermal conductivity and diffusivity of carbon-reinforced polyetherketoneketone composites. Journal of Applied Polymer Science, 136(38), 47975. doi: https://doi.org/10.1002/app.47975
12. Yee, C., Ray, M., Tang, F., Wan, J., Tatuaca, R., Natali, M., & Koo, J. H. (2014). In situ ablation recession sensor for ablative materials based on ultraminiature thermocouples. Journal of Spacecraft and Rockets, 51(6), 1789-1796. doi: https://doi.org/10.2514/1.A32926
13. Avalle, M., Belingardi, G., & Montanini, R. (2001). Characterization of polymeric structural foams under compressive impact loading by means of energy-absorption diagram. International journal of Impact Engineering, 25(5), 455-472. doi: https://doi.org/10.1016/S0734-743X(00)00060-9
14. Li, Q. M., Magkiriadis, I., & Harrigan, J. J. (2006). Compressive strain at the onset of densification of cellular solids. Journal of Cellular Plastics, 42(5), 371-392. doi: https://doi.org/10.1177/0021955X06063519